Journal of Solid State Chemistry 183 (2010) 2695–2702

Contents lists available at ScienceDirect

Journal of Solid State Chemistry

journal homepage: www.elsevier.com/locate/jssc

Heterometallic *M*/Mn (*M*=Cu, Co, Zn) acetate complexes as precursors for binary oxides

Valeriya G. Makhankova [a,*], Oleksiy V. Khavryuchenko [a], Vladyslav V. Lisnyak [a], Vladimir N. Kokozay [a], Viktoriya V. Dyakonenko [b], Oleg V. Shishkin [b,c], Brian W. Skelton [d], Julia Jezierska [e]

[a] Department of Inorganic Chemistry, Kyiv National Taras Shevchenko University, Volodymyrska street 64, Kyiv 01601, Ukraine
[b] STC "Institute for Single Crystals" National Academy of Sciences of Ukraine, 60 Lenina Avenue Kharkiv 61001, Ukraine
[c] Department of Inorganic Chemistry, V.N. Karazin Kharkiv National University, 4 Svobody sq., Kharkiv 61077, Ukraine
[d] Chemistry M313, School of Biomedical, Biomolecular and Chemical Sciences, University of Western Australia, 6009, Australia
[e] Faculty of Chemistry, University of Wroclaw, 14 F. Joliot-Curie, 50-383 Wroclaw, Poland

ARTICLE INFO

Article history:
Received 21 June 2010
Received in revised form
20 August 2010
Accepted 27 August 2010
Available online 25 September 2010

Keywords:
Heterometallic complexes
X-ray crystallography
X-ray powder diffraction
Thermogravimetric analysis
Temperature programmed desorption mass-spectrometry
SEM/EDX analysis

ABSTRACT

A facile one-pot procedure, or so-called "direct synthesis," was used to prepare the novel heterometallic complexes $[M_2Mn(OAc)_6(bpy)_2]$, where *M*=Cu (**1**), Co (**2**), Zn (**3**), bpy=2,2′-bipyridyl, with high yields *via* oxidative dissolution of pure metals in a liquid phase. The complexes were characterized by an elemental analysis, single crystal X-ray diffraction method and FTIR. These complexes are proposed as precursors, whose thermal degradation may lead to the formation of solids possessing nano- to microsize levels of dispersity. The thermal behavior of the complexes obtained was studied by thermal analysis (TG/DTA/DTG) in both air and N_2 and also by TPD mass-spectrometry *in vacuo*. The FTIR, X-ray powder diffraction (PXRD) and thermoanalytical data were used for the identification of the solid products of thermal degradation. The morphology and microstructure of the solid residues were analyzed, using scanning electron microscopy with energy dispersive X-ray microanalysis (SEM/EDX) at mkm and sub-micro levels.

1. Introduction

Recently, the growing interest in spinels and spinel-based materials has been stimulated by their application in various heterogeneous catalytic reactions [1–5]. The spinels and spinel-based composites are usually synthesized by prolonged high temperature treatment of appropriate precursors, such as mixed nitrates [6] or carbonates [7], and hydroxy-salts obtained by co-precipitation [8].

However, under high temperatures, a considerable sintering of the resultant particles is observed leading to formation of dense particles with low surface area. Such microtextural characteristics are required for preparation of dense spinel-based ceramics, but exclude their other applications in, for example, heterogeneous catalysts. Hence, the search for precursors and routes adequate for their low-temperature synthesis is an actual task.

Within this context, routes different in principle, such as the organic acid complex method [9–11] and the Pechini method [12,13] have been found to be rather promising for the spinel preparation. The common objective of these approaches is to decrease the temperature necessary for the thermal degradation.

Having the above-mentioned endeavors in mind, the present study was done to obtain the adequate precursors for convenient synthesis of the spinels at low temperatures (below 350 °C). We hoped to synthesize, examine and thermally degrade bimetallic complexes of bipyridyl and acetate ligands, which have a fixed molar ratio between two different metals and established oxygen-bonded cores that bring the metal atoms close together, as possible precursors for spinel-based materials preparation. It seems logical to suppose that thermal degradation of bimetallic complexes with easily desorbing ligands could result in the formation of self-organized systems, possessing different levels of dispersity, from nano- to micro-size, due to two driving factors of metal diversity and gaseous product evolution.

Facile one-pot procedure was used to prepare the desired coordination compounds with high yields *via* oxidative dissolution of pure metals in a liquid phase, this being the so-called "direct synthesis" method [14–17], has been used to obtain bimetallic and trimetallic complexes. A series of heterometallic complexes *M*/Mn (*M*=Cu, Co, Zn) with acetate and 2,2′-bipyridyl (bpy) has been isolated and characterized by X-ray diffraction study of single-crystals, and also by an FTIR, TPD-MS,

* Corresponding author. Fax: +380 44 2962467.
E-mail address: leram@univ.kiev.ua (V.G. Makhankova).

0022-4596/$ - see front matter © 2010 Elsevier Inc. All rights reserved.
doi:10.1016/j.jssc.2010.08.040

TG/DTA/DTG, PXRD and SEM/EDX methods. Cu and Co were chosen as pair metals to an Mn due to their ability to adopt different oxidation states, an important feature for the catalysts of various chemical processes, which include oxidative stages, while Zn was also used, since the $Cu_{0.5}Zn_{0.5}Mn_2O_4$ spinel possesses high catalytic activity in the reaction of methanol decomposition [18].

2. Experimental section

2.1. Materials and general methods

All solvents and reagents were of an analytical reagent grade and were used without further purification unless otherwise stated. Ammonium acetate was previously dried *in vacuo*. Syntheses of the complexes were carried out in air. Elemental analyses for the metals were performed with an ICP spectrometer (Fisons Instruments, ARL Model 3410+). CHN-analyses were performed with Perkin-Elmer 2400 Analyzer. Infrared (IR) spectra were recorded in the 400–4000 cm^{-1} region from KBr pellets on Bruker 113v spectrophotometer.

2.2. Synthesis of the complexes

[$Cu_2Mn(OAc)_6(bpy)_2$] (**1**): a mixture of copper powder (0.08 g, 1.25 mmol), manganese(II) acetate tetrahydrate (0.31 g, 1.25 mmol), 2,2′-bipyridyl (0.39 g, 2.5 mmol), ammonium acetate (0.38 g, 5 mmol) and CH_3OH (20 mL) were placed in a 50 mL conic flask. The reaction mixture was mechanically stirred at 50–60 °C in a system open to air for 2 h after which the total dissolution of copper was observed. The resulting hot green solution was filtered to remove small quantities of by-products, and then cooled to the room temperature. Green single-crystals suitable for X-ray analysis were successively obtained from the resultant solution after 2 days. Yield 0.43 g (82% by copper). *Anal.* Calc. for $C_{32}H_{34}Cu_2MnN_4O_{12}$: C, 45.29; H, 4.04; N, 6.60; Cu, 14.98; Mn, 6.47. Found: C, 45.3; H, 4.2; N, 6.5; Cu, 15.0; Mn, 6.7. IR (KBr discs, cm^{-1}): 3420br, 3085w, 3063w, 3028w, 2995w, 2920w, 1593vs, 1494w, 1476m, 1405s, 1373sh, 1331w, 1323m, 1247w, 1163w, 1156w, 1098w, 1042w, 1012m, 912w, 764m, 730w, 645s, 614m.

[$Co_2Mn(OAc)_6(bpy)_2$] (**2**): the synthesis of **2** was carried out similarly to **1**, using cobalt powder (0.07 g, 1.25 mmol) instead of copper. Yield 0.34 g (65% by cobalt). *Anal.* Calc. for $C_{32}H_{34}Co_2MnN_4O_{12}$: C, 45.79; H, 4.08; N, 6.67; Co, 14.04; Mn, 6.54. Found: C, 45.4; H, 4.2; N, 6.8; Co, 14.3; Mn, 6.4. IR (KBr discs, cm^{-1}): 3420br, 3090w, 3074w, 3028w, 2927w, 1592vs, 1492w, 1476m, 1444s, 1408s, 1336w, 1315w, 1252w, 1175w, 1156w, 1056w, 1042w, 1022m, 944w, 773s, 738w, 673w, 652m, 618w, 516w.

[$Zn_2Mn(OAc)_6(bpy)_2$] (**3**): the synthesis of **3** was carried out similarly to **1** using zinc powder (0.08 g, 1.25 mmol) instead of copper. Yield 0.42 g (78% by zinc). *Anal.* Calc. for $C_{32}H_{34}Zn_2MnN_4O_{12}$: C, 45.10; H, 4.02; N, 6.57; Zn, 15.34; Mn, 6.45. Found: C, 45.3; H, 4.1; N, 6.8; Zn, 15.5; Mn, 6.6. IR (KBr discs, cm^{-1}): 3420br, 3109w, 3066w, 3004w, 2928w, 1598vs, 1494w, 1477m, 1429vs, 1327m, 1250w, 1179w, 1157w, 1104w, 1060w, 1022m, 931w, 912w, 773s, 737w, 674w, 652m, 616w, 515w.

2.3. Thermal degradation of the complexes

Thermal degradation of complexes **1–3** was performed under air or argon (in static atmospheres), the prepared samples being denoted as **1–3-air** or **1–3-Ar**, respectively. In the preparation procedure of **1–3-air,** a sample of the complex (ca. 0.5 g) was placed in a glass closed-bottom cylindrical reactor (diameter 30 mm), stationed vertically in a locally constructed thermostated tube furnace. The temperatures inside the isothermal cell were monitored, using Pt/Rh thermopiles.

The complexes **1–3** were subsequently treated using a strict temperature program sequence. Initially, the samples were heated to ~250 °C until melting was observed, and then held at this temperature for 30 min. The samples were then heated to ~300 °C at which point the temperature was held for 4 h to avoid splashing the melt. Finally, the samples were heated to ~350 °C and held for 1.5 h, and then allowed to cool in air.

In the preparation procedure of **1–3-Ar,** a sample of the complex (ca. 0.5 g) was placed in a glass closed-bottom cylindrical reactor (diameter 30 mm) with polished joints with a perpendicular extension from the top. The reactor was stationed at 45° to the vertical with the perpendicular extension oriented downwards. This was connected to an Ar–vacuum line *via* the joint, evacuated, and then filled with Ar. The heating procedure was performed analogously to that of **1–3-air** samples. The bpy sublimed and deposited onto the walls of the perpendicular extension. The products of thermal degradation were left to cool under the Ar atmosphere, and then removed in air.

An additional experiment was performed with **1** in order to check the mechanism of the complexes decomposition. The complex **1** was placed on the thin macroporous glass filter stationed inside the reactor. The bottom of the reactor was outside of the heating zone, and had the room temperature. The heating was performed analogously to the above-mentioned procedures. The complex **1** has melted upon heating and completely left the heating zone through the filter with no solid residues in the filter upper part. The resulting substance (hereby **1-melt**) was studied by PXRD and FTIR (see Section 3).

2.4. X-ray structure determination

Crystallographic data, details of the data collection and processing, structure solution and refinement are summarized in Table 1. Selected bond lengths and angles for **1–3** are given in Table 2. Diffraction experiments were performed on a Bruker SMART CCD diffractometer (ω rotation scans with narrow frames) for **1** and on an Oxford Diffraction Xcalibur diffractometer (CCD detector, ω and ϕ scans), for **2** and **3.** The diffractometers were equipped with a graphite-monochromator and Mo Kα radiation (λ=0.71073 Å). The data were corrected for Lorentz polarization effects and for the effects of absorption (multi-scan method using SADABS [19] in **1** and CrysAlisRED [20] in **2, 3**). The structures were solved by direct methods and refined against F^2 by full-matrix least-squares, using the SHELX-97 package [21]. All non-hydrogen atoms were refined with anisotropic displacement parameters. The H-atoms were located from difference maps and refined by the use of "riding" models with $U_{iso}=1.5\times U_{eq}$ of the parent atom for methyl groups and $1.2\times U_{eq}$ for the remaining H-atoms).

2.5. Experimental techniques

Temperature programmed desorption mass-spectrometry (TPD-MS) measurements were performed by heating of the samples of the complexes in a high vacuum ($p<10^{-4}$–10^{-5} Pa), using a linear heating method at a rate of 0.167 °C s^{-1} rate. The resultant volatile products were analyzed using an MX 7304 A mass-spectrometer, as the detector of the desorbed species [22].

Thermal degradation was examined in dynamic atmospheres of dry nitrogen and air (flow rate of 50 mL min^{-1}), using Setaram Setsys 16/18 and Setaram Labsys 2000 instruments, respectively. TG/DTA/DTG experiments were performed on about 10 mg of sample supported in alumina crucibles. The TG/DTA/DTG curves

Table 1
Crystallographic data and refinement parameters of **1–3.**

	$[Cu_2Mn(OAc)_6(bpy)_2]$ (**1**)	$[Co_2Mn(OAc)_6(bpy)_2]$ (**2**)	$[Zn_2Mn(OAc)_6(bpy)_2]$ (**3**)
Empirical formula	$C_{32}H_{34}Cu_2MnN_4O_{12}$	$C_{32}H_{34}Co_2MnN_4O_{12}$	$C_{32}H_{34}MnZn_2N_4O_{12}$
Crystal color, morphology	Pale green, blocks	Dark-red, blocks	Yellow, blocks
Crystal system	Triclinic	Monoclinic	Triclinic
Space group	$P\bar{1}$	$C2/c$	$P\bar{1}$
a (Å)	8.0468(6)	26.910(4)	8.138(3)
b (Å)	9.5915(7)	8.672(2)	9.803(2)
c (Å)	12.5620(9)	16.288(2)	12.818(2)
α (deg)	103.633(2)	90.00	106.03(4)
β (deg)	97.684(2)	113.56(2)	97.50(3)
γ (deg)	108.329(2)	90.00	108.54(4)
V (Å^3)	871.43(11)	3484.2(12)	904.7(6)
Z	1	4	1
Formula weight (g mol^{-1})	848.67	839.43	852.31
Density (calcd) (g cm^{-3})	1.617	1.600	1.564
T (K)	150(2)	294(2)	294(2)
Absorption coefficient (mm^{-1})	1.634	1.366	1.724
F(0 0 0)	433	1716	435
θ Range (°)	1.71–37.53	2.99–30.00	2.84–27.50
Index ranges	$-13 \le h \le 13$; $-16 \le k \le 15$; $-21 \le l \le 21$	$-37 \le h \le 37$; $-12 \le k \le 12$; $-21 \le l \le 22$	$-10 \le h \le 10$; $-12 \le k \le 12$; $-16 \le l \le 16$
Reflections collected	16,877	14,488	6542
Independent reflections	8763	4926	4003
Data/restraints/params	8763/0/235	4926/0/234	4003/0/235
R_1, wR_2 [$I > 2\sigma(I)$]	0.0359, 0.0882	0.0331, 0.0790	0.0411, 0.1223
R_1, wR_2 (all data)	0.0501, 0.0942	0.0649, 0.0874	0.0550, 0.1307
GOF	1.053	0.909	1.123
Largest diff. peak, hole (eÅ^{-3})	0.906, −0.733	0.306, −0.285	0.622, −0.569

Table 2
Selected bond distances (Å) and angles (°) for **1–3**.

1		**2**		**3**	
Cu(1)–O(5)	1.9584(11)	Co(1)–O(2)	2.033(2)	Zn(1)–O(5)	2.020(2)
Cu(1)–O(1)	2.1448(12)	Co(1)–O(3)	2.042(2)	Zn(1)–O(1)	2.045(3)
Cu(1)–O(3)	2.0608(11)	Co(1)–N(2)	2.127(2)	Zn(1)–O(3)	2.068(3)
Cu(1)–N(2)	2.0539(14)	Co(1)–O(5)	2.145(2)	Zn(1)–N(2)	2.188(3)
Cu(1)–N(1)	2.1061(12)	Co(1)–N(1)	2.159(2)	Zn(1)–N(1)	2.194(3)
Mn(1)–O(2)	2.1407(11)	Co(1)–O(6)	2.314(2)	Mn(1)–O(2)	2.157(3)
Mn(1)–O(3)	2.2317(11)	Mn(1)–O(1)	2.145(2)	Mn(1)–O(3)	2.233(2)
Mn(1)–O(4)	2.1894(11)	Mn(1)–O(4)	2.192(2)	Mn(1)–O(4)	2.173(3)
O(5)–Cu(1)–O(1)	98.10(5)	Mn(1)–O(5)	2.213(2)	O(5)–Zn(1)–O(1)	98.85(12)
O(5)–Cu(1)–O(3)	98.40(5)	O(2)–Co(1)–O(3)	96.78(7)	O(5)–Zn(1)–O(3)	98.46(10)
O(1)–Cu(1)–O(3)	95.21(4)	O(2)–Co(1)–N(2)	99.70(7)	O(1)–Zn(1)–O(3)	99.43(10)
O(5)–Cu(1)–N(2)	164.00(5)	O(3)–Co(1)–N(2)	93.66(7)	O(5)–Zn(1)–N(2)	159.41(10)
O(1)–Cu(1)–N(2)	88.78(5)	O(2)–Co(1)–O(5)	103.32(6)	O(1)–Zn(1)–N(2)	88.58(10)
O(3)–Cu(1)–N(2)	95.32(5)	O(3)–Co(1)–O(5)	97.17(6)	O(3)–Zn(1)–N(2)	99.23(10)
O(5)–Cu(1)–N(1)	86.38(5)	N(2)–Co(1)–O(5)	153.13(6)	O(5)–Zn(1)–N(1)	85.88(10)
O(1)–Cu(1)–N(1)	113.11(4)	O(2)–Co(1)–N(1)	83.28(7)	O(1)–Zn(1)–N(1)	117.82(11)
O(3)–Cu(1)–N(1)	150.41(5)	O(3)–Co(1)–N(1)	168.89(7)	O(3)–Zn(1)–N(1)	141.47(10)
N(2)–Cu(1)–N(1)	77.63(5)	N(2)–Co(1)–N(1)	75.42(7)	N(2)–Zn(1)–N(1)	73.71(10)
O(2)–Mn(1)–O(4)	91.84(5)	O(5)–Co(1)–N(1)	93.61(6)	O(2)–Mn(1)–O(4)	91.53(11)
O(4)–Mn(1)–O(3)	89.60(4)	O(2)–Co(1)–O(6)	159.87(6)	O(4)–Mn(1)–O(3)	90.88(9)
O(2)–Mn(1)–O(3)	89.42(4)	O(3)–Co(1)–O(6)	94.01(6)	O(2)–Mn(1)–O(3)	88.36(9)
		N(2)–Co(1)–O(6)	96.50(6)		
		O(5)–Co(1)–O(6)	58.34(6)		
		N(1)–Co(1)–O(6)	89.35(6)		
		O(1)–Mn(1)–O(4)	93.18(6)		
		O(1)–Mn(1)–O(5)	88.29(6)		
		O(4)–Mn(1)–O(5)	88.54(6)		

were recorded at a heating rate of 5 °C min^{-1} over the temperature range 20–1000 °C.

The X-ray powder diffraction (PXRD) patterns were collected in θ–θ mode, using a DRON–4–07 diffractometer (filtered Cu-Kα_1–radiation, $\lambda = 1.5405$ Å, graphite-monochromator, 40 kV, 20 mA) in the angular range $2\theta = 10$–$90°$ in a step-scan mode with a step size of 0.04° and counting time of 2 s per data point. SiO_2 (2θ calibration) and Al_2O_3–NIST SRM1976 were used as external standards.

The residual solid products of the complexes decomposition were studied by means of scanning electron microscopy (SEM), using a Zeiss SEM Ultra60 instrument equipped with an Inca

Wave 500 Oxford energy dispersive X-ray microanalysis (EDX) system.

3. Results and discussion

3.1. Synthesis of the complexes and spectroscopic characterization

The reaction of metal powder (Cu, Co, Zn) and manganese(II) acetate with 2,2′-bipyridyl (bpy) and ammonium acetate in methanol with the molar ratio M:Mn(OAc)$_2$:bpy:NH$_4$(OAc)= 1:1:2:4 in air resulted in the formation of a transparent colored (green for **1**, dark-red for **2** and yellow for **3**) solutions. The mixed-metal compounds, which precipitated after 1–2 days, showed analytical data corresponding to the presence of Mn and M in a 1:2 stoichiometry.

The IR spectra of **1**–**3** are quite similar and typical of carboxylate complexes. The asymmetric and symmetric vibrations of the acetate groups registered as wide multi-component bands at 1590 and 1400 cm^{-1}, respectively [23]. The complex pattern indicated several types of acetate coordination, this being confirmed by the X-ray crystallography. Aromatic ν(C=C) and ν(C=N) stretching vibrations of the 2,2′-bipyridyl rings are partially obscured by broad strong absorption from the carboxylates. Peaks about 770 and 650 cm^{-1} are clearly distinguishable and assigned to CH out-of-plane bending vibrations of two adjacent H-atoms, ring breathing and deformation vibrations of the coordinated bpy.

3.2. Structural description

Complexes **1**–**3** possess similar molecular trinuclear structure (the Cu and Zn structures being isomorphous) with a linear M–Mn–M [where M=Cu (**1**), Zn (**2**), Co (**3**)] arrangement of metal atoms (Fig. 1), analogous to that reported in Refs. [24–27]. The Mn atom is located on a crystallographic inversion center and is coordinated octahedrally by six carboxylate oxygen atoms (Mn–O distances are in the range 2.1407(11)–2.233(2) Å). Four of these oxygen atoms belong to acetate groups bridging to the peripheral metal atoms in the common bidentate fashion, while two other oxygen atoms are from a rarely observed monoatomic μ_2-bridging acetate groups. In **1** and **3,** the peripheral metal atoms M are pentacoordinated by three O atoms of bridging acetate groups and two N atoms of 2,2′-bipyridyl. In contrast to **1** and **3** structures, in **2** the bridging acetate group is tridentate with the non-bridging O atom being bound to cobalt, thus completing the coordination sphere of the cobalt to six, forming distorted octahedral polyhedron. The distances M–O and M–N (M=Cu, Co, Zn) are listed in Table 2 and are in a good accordance with those reported in the literature [24–28].

3.3. Thermal studies

Volatile species formed during the dynamic thermal decomposition of **1**–**3** were examined by means of TPD-MS detecting several signal intensities. The registered profiles for mass spectra lines m/z=18 H_2O^+, 28 CO^+, 44 CO_2^+, 58 $(CH_3)_2CO^+$, 60 CH_3COOH^+, 78 $C_5H_4N^+$ and 156 $C_{10}H_8N_2^+$ were examined (Fig. 2).

According to TPD-MS, all physisorbed water volatilized below 200 °C. In **1**, the asymmetric water desorption peaks (at c.a. 80 °C) are due to molecular recombination in the gas phase, with the symmetric peaks (at c.a. 125 °C) being the result of single molecules desorbed from the surface. For **2,** symmetrical desorption peaks were observed at 95 and 135 °C, with those for **3** observed at 85 and 135 °C.

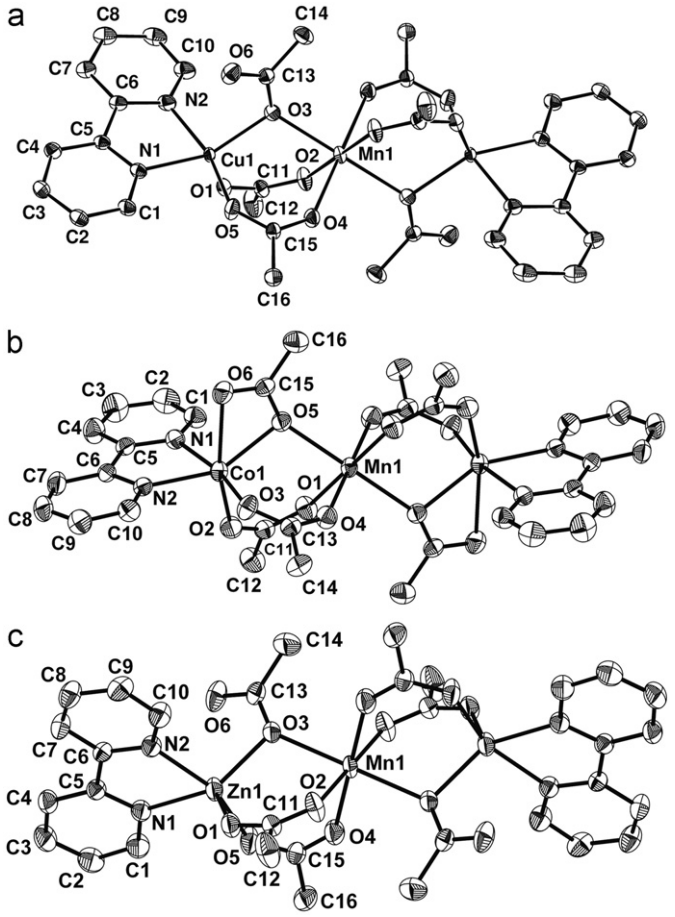

Fig. 1. Labeled ORTEP plots of the molecular structures of **1** (a), **2** (b) and **3** (c). The ellipsoids of the non-hydrogen atoms have been drawn at the 40% probability level with H-atoms omitted for clarity.

Desorption of bpy (m/z=78 $C_5H_4N^+$, 156 $C_{10}H_8N_2^+$) is recorded in the temperature region 155–400 °C (**1**), 175–400 °C (**2**), 145–350 °C (**3**). This desorption precedes removal of the acetates from the complexes. Since as at the first stage of complexes destruction, a molecular form of bpy eliminates, consequently one can consider further thermal processes as the $2M(CH_3COO)_2 \cdot Mn(CH_3COO)_2$ fragment destruction.

The destruction of acetates from the fragments of **1**–**3** occurs in the ranges 155–400 °C (**1**), 195–400 °C (**2**) and 145–350 °C (**3**). In **2** and **3,** two subsequent processes with maxima temperatures at c.a. 237 and 300 °C were detected in the MS profiles with m/z=18 H_2O^+, 28 CO^+ and 44 CO_2^+ and 58 $(CH_3)_2CO^+$. In contrast to previous observations, the destruction of acetate fragments of **1** passes through three stages with maximum temperatures at c.a. 215, 257 and 300 °C in MS profiles of m/z=28 CO^+ and 44 CO_2^+. It should be noted that two peaks at 257 and 300 °C in the MS profiles belong to acetone and its derivatives (m/z=28 CO^+, 58 $(CH_3)_2CO^+$), while peak at c.a. 215 °C belongs to acetic acid (m/z=60 CH_3COOH^+) confirming the occurrence of the following reactions, as reported earlier in Refs. [29,30]

$$Mn(CH_3COO)_2 \rightarrow MnO + (CH_3)_2CO + CO_2 \quad (1)$$

$$Cu(CH_3COO)_2 \rightarrow Cu + CH_3COOH + CO_2 + H_2 + C \quad (2)$$

The DTA, TG and DTG curves for all complexes studied in a dynamic air/N_2 atmosphere are presented in Fig. 3, and the data are summarized in Table 3. Curves are featureless until the onset

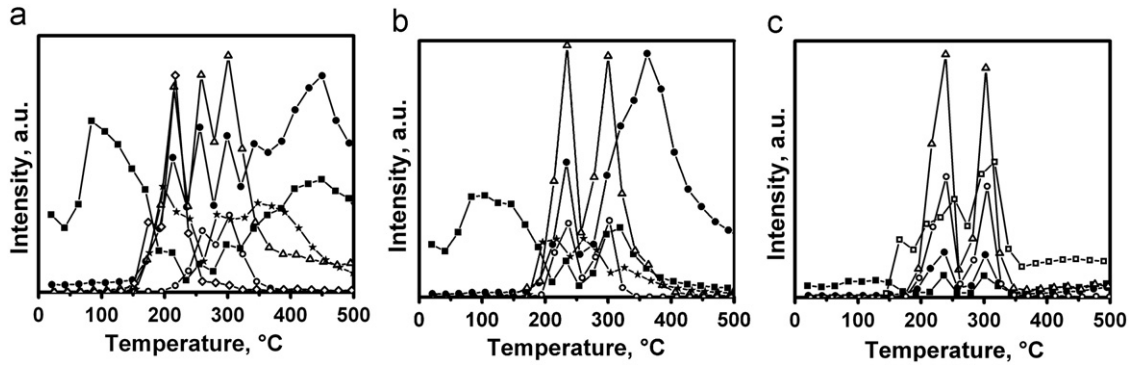

Fig. 2. TPD-MS profiles of 1 (a), 2 (b) and 3 (c) for the ions with m/z 18 H_2O^+ (■), 28 CO^+ (●), 44 CO_2^+ (△), 58 $(CH_3)_2CO^+$ (○), 60 CH_3COOH^+ (◇), 78 $C_5H_4N^+$ (⋆) and 156 $C_{10}H_8N_2^+$ (□).

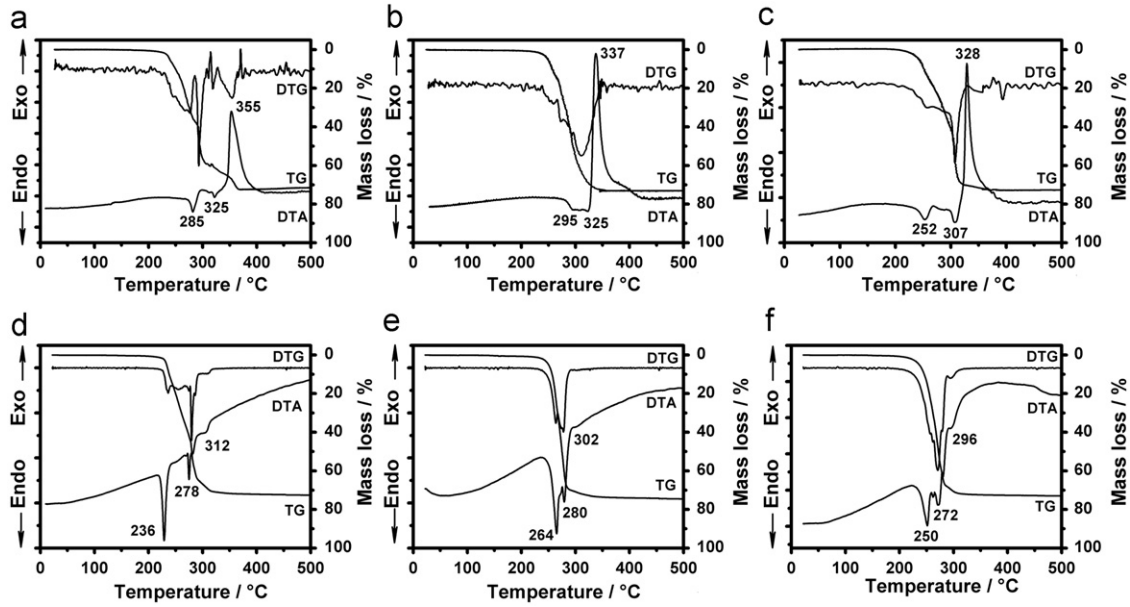

Fig. 3. TG/DTA/DTG curves of **1** (a, d), **2** (b, e) and **3** (c, f) in air and N_2 atmosphere, respectively.

of thermal decomposition at c.a. 195 °C. Above this temperature, thermal degradation of the complexes occurred in the range 195–370 °C (**1**), 210–345 °C (**2**) and 190–360 °C (**3**) with loss of two bpy molecules and six acetate residues.

The observed mass losses due to these processes are listed in Table 3. The thermal degradation of the complexes in N_2 atmosphere was accompanied by three endothermic effects. Two endothermic and one exothermic effect are recorded for the thermal degradation in air. It should be noticed that the peak temperatures for the endothermic effects are shifted to higher temperatures for the case of thermal degradation in air.

3.4. Phase composition and morphology of the thermal degradation products

The results of PXRD experiments performed on the samples, which were decomposed in air and Ar atmospheres are shown in Fig. 4. Widening of the peaks in the 2θ 10–25° region indicates the presence of amorphous phases, being more pronounced for the Co-containing oxide samples.

Thermal degradation of **1** in the air gives a mixture of crystalline hausmannite Mn_3O_4 (JCPDS 24–0734) and metallic Cu (JCPDS 04–0836) phases (85 and 15 mass%, respectively). In argon, **1** degrades to metallic Cu, Mn_3O_4 and MnO (JCPDS 07–0230) (54, 24 and 22 mass%, respectively).

Tetragonal $(Co,Mn)Mn_2O_4$ and cubic $(Co,Mn)Co_2O_4$ spinels are obtained, when **2** is degraded in air. The lattice parameter for the cubic $(Co,Mn)Co_2O_4$ phase calculated from the XRD pattern is found to be $a=8.1194$ Å, intermediate between that of Co_3O_4 (JCPDS 43–1003, sp.gr. $Fd\bar{3}m$, $a=8.084$ Å) and $MnCo_2O_4$ (JCPDS 23–1237, sp.gr. $Fd\bar{3}m$, $a=8.269$ Å). The ionic radius of Co^{2+} is smaller than Mn^{2+}, so replacement of Co by Mn leads to a linear dependence of a against x in the $(Co_{1-x}Mn_x)Co_2O_4$ solid solution. In accordance with Vegard's Law, the composition was estimated to be $(Co_{0.8}Mn_{0.2})Co_2O_4$. The c/a ratio for tetragonal spinel $(Mn_{1-x}Co_x)Mn_2O_4$ (sp.gr. $I4_1/amd$, $a=5.738$ Å, $c=9.330$ Å) was found to be 1.626 corresponding to the Vegard composition of $(Co_{0.2}Mn_{0.8})Mn_2O_4$.

Only a binary (Co,Mn)O solid solution is formed from thermal degradation of **2** in Ar. The lattice parameter for cubic $(Co_xMn_{1-x})O$ phase, calculated from the PXRD pattern, is found to be $a=4.368$ Å, intermediate between that of cubic MnO (JCPDS 07–0230, sp.gr. $Fm\bar{3}m$, $a=4.445$ Å) and CoO (JCPDS 48–1719, sp.gr. $Fm\bar{3}m$, $a=4.261$ Å). The composition $(Co_{0.4}Mn_{0.6})O$ was estimated from Vegard's Law.

According to the XRD patterns, the solid products of thermal degradation of **3** in air consist of the two crystalline

Table 3
Thermal decomposition data of the complexes 1–3.

Complex	N_2 atmosphere				Air atmosphere			
	DTA peak (°C)	Solid residue	Mass loss, %		DTA peak (°C)	Solid residue	Mass loss (%)	
			Observation	Calculated			Observation	Calculated
1	236 Endo 278 endo 312 endo	$2CuO \cdot MnO$	72.9	72.9	285 Endo 325 endo 355 exo	$2CuO \cdot 1/3Mn_3O_4$	72.1	72.2
2	264 Endo 280 endo 302 endo	$2CoO \cdot MnO$	74.1	73.7	295 Endo 325 endo 337 exo	$2/3Co_3O_4 \cdot 1/3Mn_3O_4$	72.6	71.8
3	250 Endo 272 endo 296 endo	$2ZnO \cdot MnO$	72.8	72.6	252 Endo 307 endo 328 exo	$2ZnO \cdot 1/2Mn_2O_3$	71.3	71.6

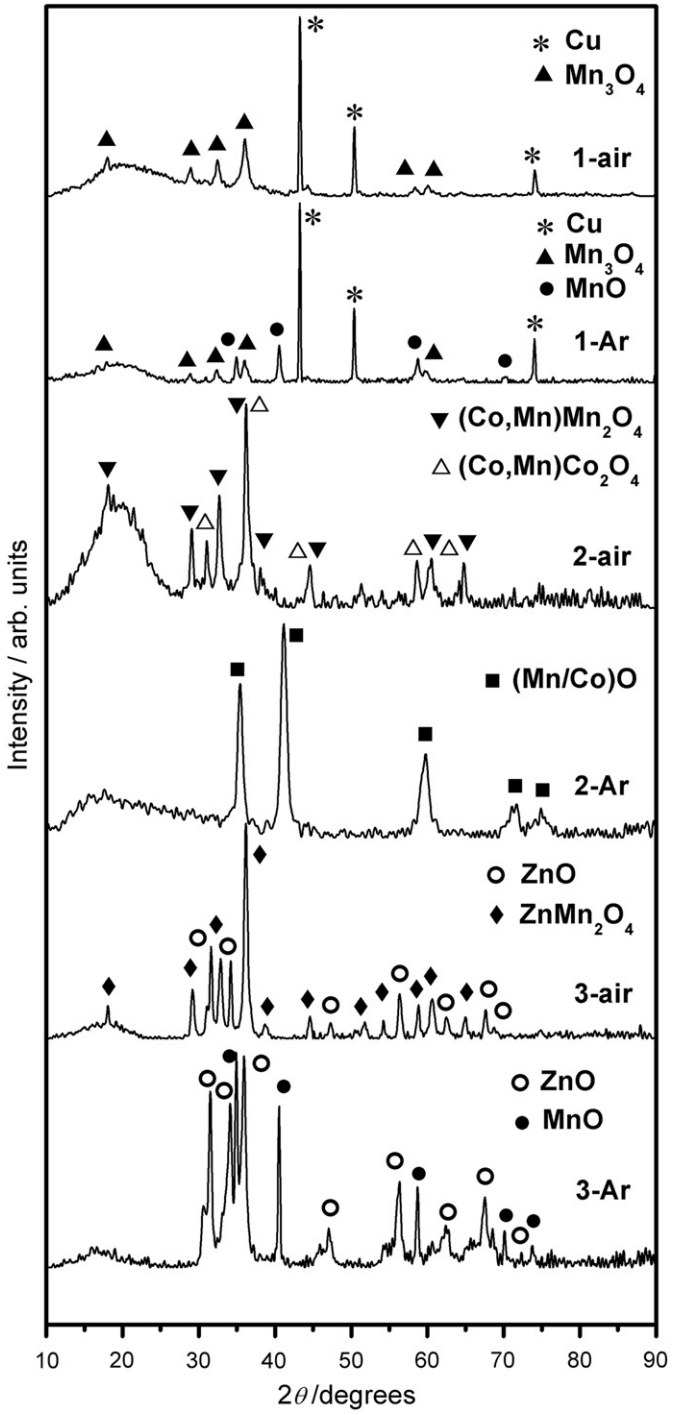

Fig. 4. PXRD patterns of solid products obtained by thermal degradation of complexes **1**–**3** in air (**1**–**3-air**) and Ar atmosphere (**1**–**3-Ar**).

phases: zincite ZnO (JCPDS 36–1451) and $ZnMn_2O_4$ (JCPDS 77–0470) (43 and 57 mass%, respectively). In contrast, the thermal degradation in Ar leads to the formation of ZnO and MnO (JCPDS 07–0230) mixture (55 and 45 mass%, respectively).

Scanning electron microscopy (SEM) showed that all the samples obtained contain mainly 100–200 non-dense mkm-sized agglomerated composites of micron-sized particles. The latter comprise nanoparticles, clearly seen in the majority of cases.

The SEM microphotographs of the sample **2-air** demonstrate the surface morphology, the microstructure of mkm particle inner volume and nano-organized particles are shown in Fig. 5. According to EDX data, Mn, Co and O are the major constituents of the sample. The EDX analysis shows a broad distribution of the Co and Mn content through the sample oscillating around an Mn:Co:O ratio of 1:2:4–2:1:4. Hence, it can be concluded that the particles, whose chemical composition is close to those of the Co- and Mn-based spinels $(Co,Mn)Co_2O_4$ and $(Co,Mn)Mn_2O_4$ are the primary crystalline phases, this being in accordance with the X-ray powder diffraction results. Micron sized agglomerates formed from the Co- and Mn-based spinel particles show a size distribution of–300 mkm. Fig. 5b presents the non-dense inner volume of the 200 μm agglomerates and the pores, which have a diameter of approximately several mkm, indicating the poor crystalline nature of the sample. The morphology of the spinel nanoparticles is shown in Fig. 5a. The majority of the spinel nanoparticles appear to be spherical, with particle sizes ranging from 30 to 200 nm, with the prevalence in the 60 and 90 nm range. Smoothing of the faceted grains of the spinel crystallites, which have pronounced polyhedral morphology, is due to the thermal degradation and an effect of the bpy melt on the crystal growth. As can be seen from Fig. 5a, small nanoscale crystallites tend to agglomerate into larger aggregates of a few hundred nanometers. The electrostatic aggregation is caused by the dipolar nature of each of the crystallites.

The SEM microscopic examination of solid residues obtained by thermal degradation of **3** in Ar was performed at micro- and sub-micro levels. It has been determined from the combination of the PXRD, SEM and EDX results that the main mkm-sized particles observed (Fig. 6) belong to ZnO (zincite). The zincite forms layered microparticles (Fig. 6a), whose dimensions varied in the range 120–500 mkm, and are easily identified from SEM micrographs and by an EDX analysis. The zincite mkm particles have low crystallinity and show a developed surface layer. This surface layer is decorated with MnO tetrahedral crystalline nanoparticles, with dimensions of c.a. 200 nm, and also with 2 mkm torroid-like particles. The latter are organized from spherical shape nanoparticles, formed due to smoothing of the faceted crystallite grains (Fig. 6b–d). To the best of our knowledge, this is the first report of the torroid-like aggregates (Fig. 6c) and tetrahedral nanoparticles (Fig. 6d) of an MnO.

According to the data of the single crystal X-ray analysis, FTIR, DTG/DTA, TPD-MS, PXRD and SEM microscopy, one can describe the process of the oxide phases formation on thermal degradation of **1**–**3** as follows.

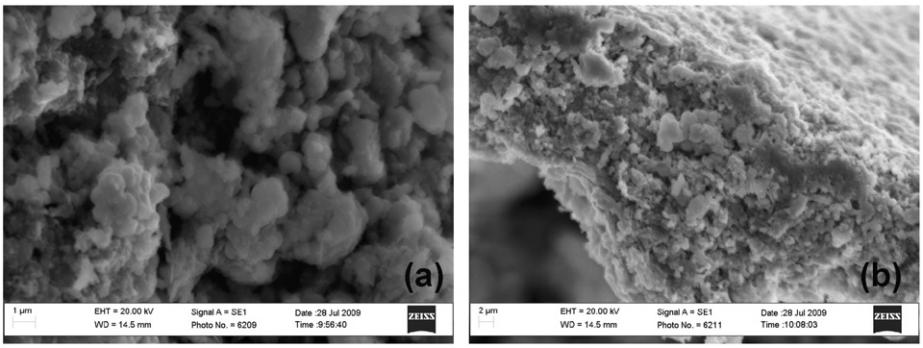

Fig. 5. SEM micrographs of **2-air**.

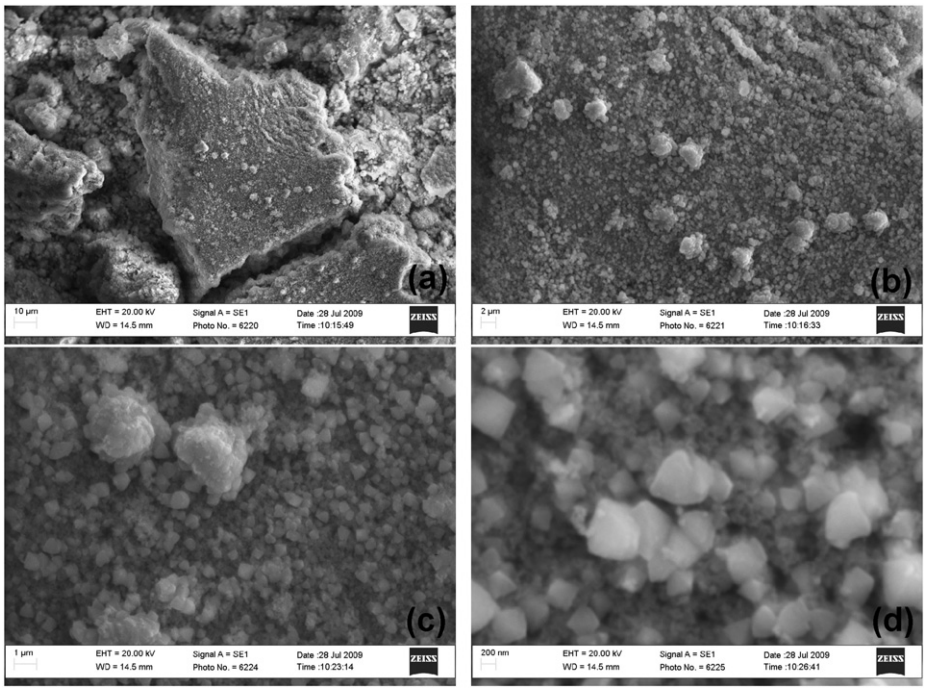

Fig. 6. SEM micrographs of **3-Ar**.

The complexes melt in the temperature range 220–270 °C, retaining molecular structure (according to the FTIR and PXRD data, which are similar for **1** and **1-melt**). Partial decomposition of acetates is also observed at this step, conjugated with bpy sublimation. The specific pathway of each complex decomposition at 270–350 °C depends on the nature of the metal.

The molecules of complex in the melt **2** polymerize upon sublimation of dipy. This leads to solidification of the melt and formation of condensed phase with homogeneous distribution of Co^{2+} and Mn^{2+}. Further decomposition of the solid mixed acetate, accompanied by acetone elimination leads to the formation of mixed *M*(II) oxide. Since CoO and MnO crystallize in the same space group ($Fm\bar{3}m$), the substituted solution (Co,Mn)O phase arises. Nucleation of (Co,Mn)O occurs upon thermal degradation of the solid mixed acetate. Since the volume of the oxide particles is lower than the volume of corresponding acetate particles and volatile products preventing the coalescence, the separation of the nano-particles takes place. Further pathway depends on the presence of oxygen. The particles of **2-Ar** aggregate upon thermal treatment and produce conglomerate of 30–200 mkm in size. In air (**2-air**), the particles are oxidized to spinels (Co,Mn)Co_2O_4 and (Co,Mn)Mn_2O_4, which also aggregate into larger formations, analogously to (Co,Mn)O.

Since hexagonal ZnO (sp.gr. $P6_3mc$) and cubic MnO (sp.gr. $Fm\bar{3}m$) belong to non-consistent space groups, and thus cannot co-crystallize, the submicro-sized particles of these oxides segregate upon decomposition of the mixed acetate. In an Ar atmosphere, the ZnO particles presumably aggregate into larger formations, while MnO particles self-organize on their surface, as can be observed in the SEM images (Fig. 6). In **3-air**, the MnO submicro-sized particles are partially oxidized, and then react with the neighboring ZnO particles to produce the $ZnMn_2O_4$ phase. Since the Zn:Mn ratio in the precursor is 2:1, the excessive ZnO remains as the separate phase.

The most complex and obscure way of decomposition is observed for **1** thermal degradation. Metallic copper is produced at the very first stages of the mixed acetate decomposition, as can be evidenced by an acetic acid evaluation, along with the MnO particles formation by the "acetone route" (as in the previous cases). For some reasons, that require additional studies, submicro-sized metallic Cu particles are not oxidized upon thermal treatment in air. Also, some copper(II) acetate decomposes by the "acetone route", too, since the resulting CuO is the only reasonable source of the oxygen for the further formation of Mn_3O_4 in **1-Ar**. In **1-air**, the MnO particles are oxidized to Mn_3O_4 spinel phase analogously to the above-mentioned case of **3-air**.

Significant amount of the spinel phase particles, organized on sub-micro and micro levels in the products of thermal decomposition of **1**–**3**, makes them promising candidates for producing composite catalysts of red/ox processes. Using the data of the present study, one can propose a generalized route of analogous heterometallic complexes transformation into oxides by the thermal treatment.

4. Conclusions

Mn-containing complexes $[M_2Mn(OAc)_6(bpy)_2]$, where M=Cu (**1**), Co (**2**), Zn (**3**), were obtained *via* convenient procedures, and were characterized with single crystal X-ray crystallography and an FTIR spectroscopy. The thermal degradation of these complexes was performed in both Ar and air atmospheres, and the processes occurring at thermal degradation were examined by means of TPD-MS and TG/DTA/DTG techniques. It was found that the formation of oxide phases on thermal degradation occurred at relatively low temperatures (below 350 °C). The SEM/EDX studies demonstrated that the degradation products are dispersed oxide systems possessing both micro- and submicro-levels of organization. The X-ray powder diffraction confirmed that the degradation products (in the case of **2** and **3**) contain significant amount of Mn spinel phases. Consequently, one can assume that M/Mn complexes obtained can be useful as a cheap-and-easy route for preparation of the precursors to be adapted for the production of heterogeneous oxidation processes catalysts.

Supplementary data

Crystallographic data for the structural analysis have been deposited with the Cambridge Crystallographic Data Center, CCDC numbers 772596 (**1**), 765511 (**2**) and 765512 (**3**). These data can obtained free of charge via http://www.ccdc.cam.ac.uk/data_request/cif or from The Cambridge Crystallographic Data Center, 12 Union Road, Cambridge CB2 1EZ, UK (Fax: +44 1223 336033; e-mail: deposit@ccdc.cam.ac.uk).

Acknowledgment

This work was supported in part by the Fundamental Research fund of Ukraine (Project 28.3/017).

References

[1] Y. Tanaka, T. Takeguchi, R. Kikuchi, K. Eguchi, Appl. Catal. A 279 (2005) 59–66.
[2] T.R. Hinklin, J. Azurdia, M. Kim, J.C. Marchal, S. Kumar, R.M. Laine, Adv. Mater. 20 (2008) 1373–1375.
[3] T.-J. Yoon, J.S. Kim, B.G. Kim, K.N. Yu, M.-H. Cho, J.-K. Lee, Angew. Chem. Int. Ed. 44 (2005) 1068–1071.
[4] J.F. Marco, J.R. Gancedo, M. Gracia, J.L. Gautier, E.I. Rios, H.M. Palmer, C. Greaves, F.J. Berry, J. Mater. Chem. 11 (2001) 3087–3093.
[5] A. Wöllner, F. Lange, H. Schmelz, H. Knözinger, Appl. Catal. A 94 (1993) 181–203.
[6] P. Peshev, A. Toshev, G. Gyurov, Mater. Res. Bull. 24 (1989) 33–40.
[7] G.H. Li, L.Z. Dai, D.S. Lu, S.Y. Peng, J. Solid State Chem. 89 (1990) 167–173.
[8] Z.P. Xu, H.C. Zeng, Chem. Mater. 12 (2000) 2597–2603.
[9] S. Sato, F. Nozaki, T. Nakayama, Appl. Catal. A 139 (1996) L1–L4.
[10] Y. Hui, Y. Huaquan, L. Yinlin, L. Neng, L. Bingxiong, J. Power Sour. 62 (1996) 223–227.
[11] W. Wang, H. Zhang, G. Lin, Z. Xiong, Appl. Catal. B 24 (2000) 219–232.
[12] M. Kakihana, M. Arima, M. Yoshimura, N. Ikeda, Y. Sugitani, J. Alloys Compd. 283 (1999) 102–105.
[13] L. Gama, M.A. Ribeiro, B.S. Barros, R.H.A. Kiminami, I.T. Weber, A.C.F.M. Costa, J. Alloys Compd. 483 (2009) 453–455.
[14] V.N. Kokozay, O.Yu. Vassilyeva, Trans. Met. Chem. 27 (2002) 693–699.
[15] A.D. Garnovskii, B.I. Kharissov, Direct Synthesis of Coordination and Organometallic Compounds, Elsevier, Amsterdam, 1999.
[16] D.S. Nesterov, V.G. Makhankova, O.Yu. Vassilyeva, V.N. Kokozay, L.A. Kovbasyuk, B.W. Skelton, J. Jezierska, Inorg. Chem. 43 (2004) 7868–7876.
[17] V.G. Makhankova, A.O. Beznischenko, V.N. Kokozay, R.I. Zubatyuk, O.V. Shishkin, J. Jezierska, A. Ozarowski, Inorg. Chem. 47 (2008) 4554–4563.
[18] S.T. Yong, K. Hidajat, S. Kawi, Catal. Today 131 (2008) 188–196.
[19] SADABS, Siemens X-ray Instruments, Madison, WI (1995).
[20] CrysAlisRED. Oxford Diffraction, Oxford, UK (2009).
[21] G.M. Sheldrick, Acta Crystallogr. A 64 (2008) 112–122.
[22] V.A. Pokrovskiy, J. Therm. Anal. Cal. 62 (2000) 407–415.
[23] K. Nakamoto, in: Infrared and Raman Spectra of Inorganic and Coordination Compounds, sixth ed., Wiley, NJ, 2009.
[24] B.-H. Ye, X.-M. Chen, F. Xue, L.-N. Ji, T.C.W. Mak, Inorg. Chim. Acta 299 (2000) 1–8.
[25] R.L. Rardin, P. Poganiuch, A. Bino, D.P. Goldberg, W.B. Tolman, Sh. Liu, S.J. Lippard, J. Am. Chem. Soc. 114 (1992) 5240–5249.
[26] S. Ménage, S.E. Vitols, P. Bergerat, E. Codjovi, O. Kahn, J.-J. Girerd, M. Guillot, X. Solans, T. Calvet, Inorg. Chem. 30 (1991) 2666–2671.
[27] S.G. Baca, Yu. Sevryugina, R. Clérac, Iu. Malaestean, N. Gerbeleu, M.A. Petrukhina, Inorg. Chem. Commun. 8 (2005) 474–478.
[28] V.W.-W. Yam, Y.-L. Pui, K.-K. Cheung, Inorg. Chem. 39 (2000) 5741–5746.
[29] M. Afzal, P.K. Butt, H. Ahrnad, J. Therm. Anal. 37 (1991) 1015–1023.
[30] K. Györyovfá, V. Balek, J. Therm. Anal. 40 (1993) 519–532.